Islamic Azad University

Journal of
Optoelectronical Nanostructures

Autumn 2023 / Vol.8, No.4

Research Paper

Investigating the Photocarrier Transmission Mechanism and the Effect of the Deposition Conditions on IBC-SHJ Solar Cell Efficiency

Pegah Paknazar[1], Maryam Shakiba*[,2]

[1]Jundi-Shapur University of Technology, Dezful, Iran.
[2]Department of Electrical and Computer Engineering, Jundi-Shapur University of Technology, Dezful, Iran.

Received: 21 Oct. 2023
Revised: 15 Nov. 2023
Accepted: 1 Dec. 2023
Published: 15 Dec. 2023

Use your device to scan and read the article online

Keywords:
Short-circuit current density, Open-circuit voltage, Fill factor, Cell efficiency, IBC-SHJ solar cell

Abstract :

In this research, the photocarrier transmission mechanism and the effect of the deposition conditions on the IBC-SHJ cell efficiency have been studied. In this regard, short-circuit current density, open-circuit voltage, fill factor and cell efficiency values have been extracted using J–V curves for various deposition parameters. The optimization of the front SRV, the thickness and doping concentration of the c-Si substrate, the thickness and doping concentration of i-a-Si layers, the doping concentration of the emitter region, the width and the doping concentration of the n- and p-strip, the gap width between electrodes and the doping concentration of the BSF region have been carried out to achieve optimum efficiency in the IBC-SHJ solar cell. In addition, the investigation of the electric field distribution in photocarrier transmission to the interdigitated back contacts has also been comprehensively studied. The results show that the n- and p-stripe width and their doping concentration were the most influential parameters for efficiency improvement. Finally, the cell efficiency of improved IBC-SHJ structure achieved 23.52%.

Citation: Pegah Paknazar, Maryam Shakiba. Investigating the Photocarrier Transmission Mechanism and the Effect of the Deposition Conditions on IBC-SHJ Solar Cell Efficiency. **Journal of Optoelectronical Nanostructures. 2023; 8 (4): 25-50. DOI: 10.30495/JOPN.2023.32064.1293**

***Corresponding author:** Maryam Shakiba
Address: Department of Electrical and Computer Engineering, Jundi-Shapur University of Technology, Dezful, Iran, **Tell:** 00989126174650 **Email:** shakiba@jsu.ac.ir

1. INTRODUCTION

As a renewable energy, solar panels have the advantages of wide application and low maintenance costs compared to wind power, biomass and other renewable power generations. In this regard, widespread deployment of solar photovoltaics (PVs) is crucial to meet growing energy demand in the world and to preserve the environment in the future [1-3]. So far, extensive researches have been done to increase the efficiency of silicon solar cells with standard finger contact structures [4-6]. In this structure, design of tandem cells and new technologies of materials and alloys used in different layers have increased efficiency [7-9]. In recent years, the design of the contact geometry of the cell has been one of the areas of interest for researchers to achieve optimal efficiency [10-12]. Among the most important structures presented in this field is the silicon heterojunction solar cell with interdigitated back contacts (IBC-SHJ) [13-15]. In this regard, placing all the contacts behind the cell removes the shadow effect and increases the short-circuit current. During the last ten years, some research have been carried out to increase the efficiency of interdigitated back contact (IBC) solar cells. Modelling of planar and pyramidal textured IBC solar cells has been developed by using Silvaco software in 2021 [16]. This paper has investigated the improvement of surface texturing with two dimensional structures in the IBC solar cell. The result have shown that the efficiency of textured surface IBC solar cell reach to 22.31% [16]. In research [17], IBC n-type silicon solar cells were fabricated with a different doping concentration of front surface layer. Also, the influence of the front surface doping level was studied via simulation. The optimum doping concentration of 4.8×10^{19} cm^{-3} was caused the highest efficiency of 20.88%. In this research, the achieved experimental result was agreed with those of the simulation data [17].
Also, the presence of heterojunction in this structure leads to an increase in the open circuit voltage due to the better passivation of the surface using the intrinsic hydrogenated a-Si buffer layer [18]. In 2013, Silvaco presented the IBC-SHJ cell with an efficiency of 20.43% [19]. In 2016, M. Belarbi and colleagues achieved an efficiency 23.20% by improving cell deposition parameters [20]. By adding more layers and anti-reflection coatings on the front side and repeating the periodicity of the structure on the back side of the cell, an efficiency of 26.30% for the IBC-SHJ structure was presented by K. Yoshikawa et al. in 2017 [21]. By considering the periodicity of the IBC-SHJ structure and, simultaneously adding more layers and anti-reflection coatings in the front side and also using TCO layers in the back part of the cell, the efficiency of 27.41% was obtained by J. Bao and colleagues in 2020 [22]. However, it should be noted that an increase in efficiency in research [21] and [22] will require an increase in the complexity of the structure and, as a result, an increase in the challenges of the fabrication process. In this research, the purpose is to design and simulate an improved silicon

heterojunction solar cell with interdigitated back contacts, in a way that has the simplest structure among different structures and obtains the most minor challenge in the fabrication process. To model the IBC-SHJ solar cell, ATHENA, and ATLAS toolboxes have been used, respectively, to deposit different layers of the cell and simulate its electrical behavior in Silvaco software. In order to increase the accuracy in simulating the structure, the trap levels of the amorphous silicon layers have been modeled. Also, MATLAB software has been used to draw the graphs as best as possible. In the second part of this research, the investigation and analysis of photo carrier transfer mechanisms in the IBC-SHJ cell are presented. In the third part, the mathematical relations governing the particle transfer and modeling of light radiation to the cell have been investigated. In the fourth part, the effect of different deposition parameters including the front surface recombination velocity (SRV), the thickness and doping concentration of the c-Si substrate, the thickness and doping concentration of the i-a-Si layer, the width, and doping concentration of the n- and p-strip and the gap width between electrodes on the characteristic solar cell outputs including Jsc, Voc, FF and η have been analyzed and investigated. In the fifth section, the most important results obtained from the IBC-SHJ cell structure are expressed and the solar cell structure with the highest efficiency, 23.52%, compared to the similar type in the reference [20] is presented.

2. ANALYSIS OF ELECTRIC FIELD DISTRIBUTION AND ITS EFFECT ON CARRIER TRANSPORT

In order to create anode and cathode electrodes, a structure of n- and p-type layers of hydrogenated a-Si are deposited on the back side of the IBC-SHJ cell so that the layers are in between. Depending on the different level doping concentration of the c-Si substrate, these n- and p-type layers, play the role of an emitter or back surface field (BSF). As shown in Fig. 1, the width of the elementary structure (pitch) of the cell is equal to the distance between the opposite electrodes, considering the gap between them. It is possible to create periodicity in more complex structures, which will face more challenges in fabrication process. In this research, the dimensions and types of materials used in different layers have been selected based on reproducibility, so that the simulation results are effective in improving the fabrication process [23]. The parameters of the IBC-SHJ cell used in the simulation are shown in Table I.

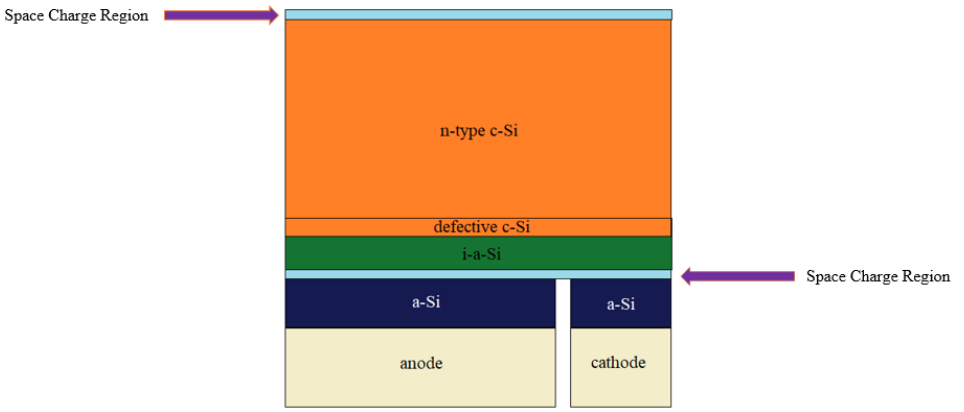

Fig. 1. Schematic of the simulated IBC-SHJ structure along with the approximated regions of space charge in the upper and lower areas of the cell

TABLE I
PARAMETERS USED IN ATHENA AND ATLAS SIMULATORS FOR IBC-SHJ SOLAR CELL

Layers	Parameters
ARC/SiN_x	Thickness = 75 nm
Bulk/c-Si(n)	Thickness = 150 µm Carrier lifetime = 7 ms Resistivity = 1 Ω.cm Band gap = 1.12 eV
Defective c-Si	Thickness = 0.001 µm Carrier lifetime = 7 ms
i-a-Si	Thickness = 0.006 µm Electron mobility = 5 $cm^2.V^{-1}.s^{-1}$ Hole mobility = 1 $cm^2.V^{-1}.s^{-1}$ Valence band density = 3×10^{20} cm^{-3} Conduction band density = 3×10^{20} cm^{-3} Affinity = 3.86 eV Permittivity = 11.9 F/m Band gap = 1.64 eV

Emitter/a-Si	Thickness = 0.02 µm Electron mobility = 5 $cm^2.V^{-1}.s^{-1}$ Hole mobility = 1 $cm^2.V^{-1}.s^{-1}$ Valence band density = 3×10^{20} cm^{-3} Conduction band density = 3×10^{20} cm^{-3} Affinity = 3.86 eV Permittivity = 11.9 F/m Band gap = 1.7 eV
BSF/a-Si	Thickness = 0.02 µm Electron mobility = 5 $cm^2.V^{-1}.s^{-1}$ Hole mobility = 1 $cm^2.V^{-1}.s^{-1}$ Valence band density = 3×10^{20} cm^{-3} Conduction band density = 3×10^{20} cm^{-3} Affinity = 3.86 eV Permittivity = 11.9 F/m Band gap = 1.7 eV
Electrodes/Al	Thickness = 0.2 µm

The substrate used to optimize deposition parameters is an n-type c-Si wafer with a thickness of 300 µm and a width of 1750 µm, which is equivalent to one cell pitch. The resistivity of the substrate is equal to 2 Ω.cm. Also, using n-type c-Si substrate will lead to an increase in Voc as a result of increasing efficiency [24] [25]. On the front surface of the cell, a SiN_x layer with a thickness of 75nm has been used as an anti-reflection coating, for this purpose, the physical model of CONMOB* has been used in the simulation. The maximum photo generation rate occurs in the upper part of the cell and is defined according to (1) [26]:

$$G = \alpha N_0 e^{-\alpha x} \quad (1)$$

In equation (1), G is the photo generation rate, N_0 is the photon flux at the surface and x is the depth of the corresponding photo generation value. α represents the absorption coefficient and is expressed according to the following relation [26]:

* Concentration Mobility

$$\alpha = 4\pi k/\lambda \quad (2)$$

In relation (2), k and λ express the extinction coefficient and the wavelength of the radiation light, respectively.

Therefore, due to not choosing the same type of impurity for ARC layers and C-Si substrate, the existence of an electric field on the top of the cell that leads to more drift of the photocarriers and prevents their recombination will be inevitable. According to Fig. 1, the presence of anti-reflection coating with the opposite doping concentration of the substrate leads to the creation of a space charge region in the front part of the cell. The internal electric field created in this space charge region will prevent the recombination of the generated photocarriers and move them toward the back contacts of the cell. Also, near the back contacts, due to the presence of the back p-n junction, another space charge region is created, which facilitates the drift of the carriers towards the anode and cathode electrodes, and by preventing the recombination of photocarriers, it will increase the photocurrent of the cell. In fact, the design of two space charge areas in the upper and lower parts of the cell, in addition to preventing the recombination of photocarriers, leads to drift them towards the interdigitated back contacts.

As shown in Fig. 2, the photocarriers generated in front part of the cell, drift towards the contacts with a similar doping concentration, under influence of electric field of space charge region. Photocarriers move vertically, towards the back contacts via the body part, and laterally, nearby the contacts. Meanwhile, the larger the cell width, the more lateral distance the carriers travel to accumulate at the contact of the same name; therefore, as the cell width increases, the recombination probability increases, in addition the cost of the fabrication increases [27].

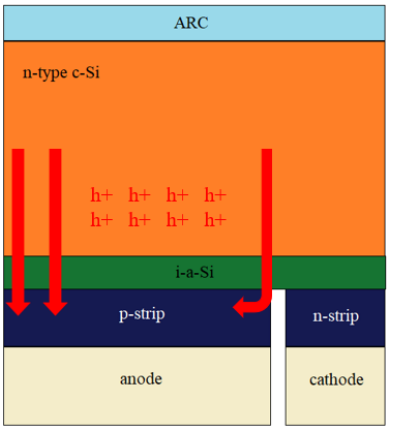

Fig. 2(a). Vertical and lateral traveling of minority carriers in IBC-SHJ cell

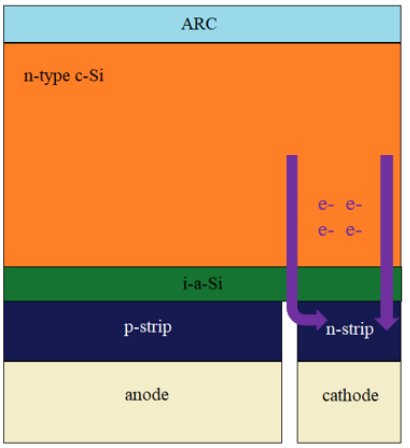

Fig. 2(b). Vertical and lateral traveling of majority carriers in IBC-SHJ cell

The electric field distribution of the IBC-SHJ solar cell structure is shown in Fig. 3. According to this figure, in the front part of the cell where there is the maximum photo generation rate, the electric field increases so that the photocarriers are separated and reach the back contacts with the lowest recombination rate. Also, according to this figure, the electric field reaches its maximum value near the back contacts; because in this part of the structure, the number of carrier collection in metal contacts must reach its highest value. Therefore, the electric field must be large enough to collect more photocarriers at the metal contacts by separating them as much as possible.

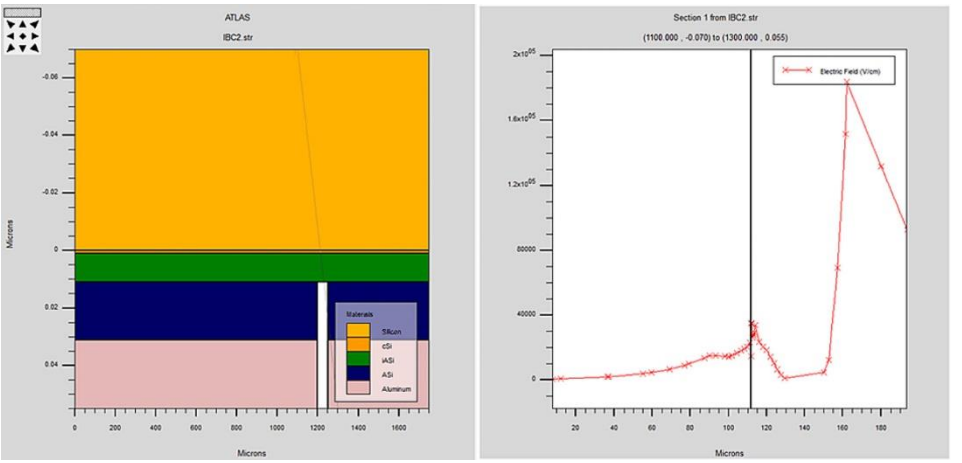

Fig. 3. Electric field distribution graph

3. PHYSICAL MODELS AND EQUATIONS USED IN SIMULATION

A. Physical models

In order to match the numerical modeling and experimental results as much as possible, in this research, we have tried to use accurate physical models to describe the behavior of IBC-SHJ cells. In this regard, the BGN[†] model has been used to reduce the energy gap [19]. In fact, the narrowing of the band gap shows how applying a high doping concentration (greater than 10^{18} cm^{-3}) changes the band gap by reducing the conduction band and increasing the valence band [28]. On the other hand, in order to model different recombination mechanisms, Fermi, SRH, Auger and surface recombination models are also included in the simulation. Meanwhile, carrier recombination is also used as a function of doping concentration via SRH and Auger mechanisms. Disordered materials such as amorphous silicon contain many defect states in their energy band gap. Therefore, the density of state (DOS) model in the energy bandgap is used to model amorphous silicon devices. The density model of the defect states is described as a combination of the tail of the band using the exponential decay function and the band' mid using the Gaussian distribution function.

For the c-Si/a-Si interface on the back surface, the thermionic emission model has been used, in which the distribution function of the defect states at the interface of two layers, one for holes and the other for electrons, is modeled. In order to model the interface between the defects-free crystalline silicon layer and

[†] Band Gap Narrowing

the amorphous silicon layer as much as possible, a defective c-Si thin layer has been used between the two layers [29]. The Sopra database is also used for the refractive index of a-Si layers [19]. AM1.5G solar spectrum has been used to simulate sunlight in standard conditions with a light intensity of 1000 w/m^2 and a temperature of 26˚C.

B. Equations of carrier transport and light radiation

The specialized software used in this research to design and simulate the IBC-SHJ solar cell is Silvaco software. The specialized software used in this research to design and simulate the IBC-SHJ solar cell is Silvaco software. The Athena tool software models and simulates the fabrication process in the Monte Carlo method and in conditions very similar to the new technologies presented in the field of semiconductor device fabrication. In addition, the Atlas tool simulates the electrical behavior of cells designed in Athena. It uses the drift-diffusion model based on the discretization of differential equations and solving equations using numerical solutions such as Gumel, Newton-Raphson and Block methods. Some of the output parameters of the Atlas tool are: Fill Factor (FF) and Efficiency (η) obtained from relations (3) and (4) respectively [26]:

$$FF = \frac{V_{mpp} I_{mpp}}{V_{oc} I_{sc}} \tag{3}$$

$$\eta = \frac{P_{out}}{P_{in}} = \frac{V_{oc} I_{sc} FF}{P_{light}} \tag{4}$$

In relation (3), V_{mpp} and I_{mpp} represent the voltage and current at the maximum power point, respectively.

Three sets of basic equations are used to simulate the solar cell in the Silvaco software based on the drift-diffusion model. These equations are: Poisson's equation, carrier's continuity equations and transport (current) equations. Poisson's equation specifies the relationship between electrostatic potential (ψ) and the space charge density (ρ) and is expressed as follows [26]:

$$div(\varepsilon \nabla \psi) = -\rho \tag{5}$$

In relation (5), ε is the permeability coefficient of the environment. The local space charge density represents carriers (electrons and holes) and ionized

impurities. On the other hand, carriers continuity equations specify the gradient of electron and hole carriers in terms of time and are defined as follows [19]:

$$\frac{\partial n}{\partial t} = \frac{1}{q} div\overrightarrow{J_n} + G_n - R_n \quad (6)$$

$$\frac{\partial p}{\partial t} = -\frac{1}{q} div\overrightarrow{J_p} + G_p - R_p \quad (7)$$

In relations (6) and (7), n and p are electrons and holes concentration respectively. J Indicates the current density, G indicates the photo generation rate and R indicates the recombination rate for the respective carriers. Electric charge is also represented by q. Also, the transport equations that determine the gradient of electron and hole carriers in terms of location, are defined as follows [19]:

$$\overrightarrow{J_n} = q\mu_n nE + qD_n \nabla n(x) \quad (8)$$

$$\overrightarrow{J_p} = q\mu_p pE - qD_p \nabla p(x) \quad (9)$$

In relations (8) and (9), μ_n and μ_p are electron and hole mobilities, respectively, E is the electric field and D_n and D_p are electrons and holes diffusion coefficients, respectively.

The equations of radiation of light rays to the IBC-SHJ are also modeled and simulated in Silvaco using Fresnel's equations. In the ray tracing optical model, the reflected and transmitted rays from the cell surface are calculated based on Fresnel's equations [30]. The simplified Fresnel's equations with Snell's laws are as follows [30]:

$$r_p = -\frac{\tan(\theta_i - \theta_t)}{\tan(\theta_i + \theta_t)} \quad (10)$$

$$t_p = \frac{2\sin\theta_t \cos\theta_i}{\sin(\theta_i + \theta_t)\cos(\theta_i - \theta_t)} \quad (11)$$

$$r_s = -\frac{\sin(\theta_i - \theta_t)}{sin(\theta_i + \theta_t)} \quad (12)$$

$$t_s = \frac{2\,sin\,\theta_t\,cos\,\theta_i}{sin(\theta_i + \theta_t)} \quad (13)$$

In relations (10) to (13), r_p and r_s represent the reflection of p and s polarized rays. Also, t_p and t_s indicate the transmission of p and s polarized rays. θ_i And θ_t express the angles of incoming and transmitted light relative to the surface average vector.

4. RESULTS AND DISCUSSION

In this research, in order to improve the characteristics of the IBC-SHJ cell, the characteristics of the different layers, including the front SRV, the thickness and doping concentration of the c-Si substrate, the thickness and doping concentration of the i-a-Si layer, the doping concentration of emitter region, the width and doping concentration of the n- and p-strip, the gap width between electrodes and the doping concentration of BSF region are optimized.

In the following, the influence of the mentioned parameters on the output characteristics of Jsc, Voc, FF and η is investigated to improve the efficiency of the IBC-SHJ solar cell. It should be noted that to investigate the effect of each parameter, other parameters of the cell are considered constant.

A. Effect of front SRV

According to the explanations provided in the second part, the maximum number of photo generation occurs at a short distance from the cell surface. Therefore, SRV will be a limiting factor in the photocurrent of the cell, so that the presence of a low density of trap surfaces leads to a reduced probability of trapping of the generated photocarriers. The current-voltage curve and graphs of Jsc, Voc, FF and η according to the change of front SRV are presented in Fig. 4.

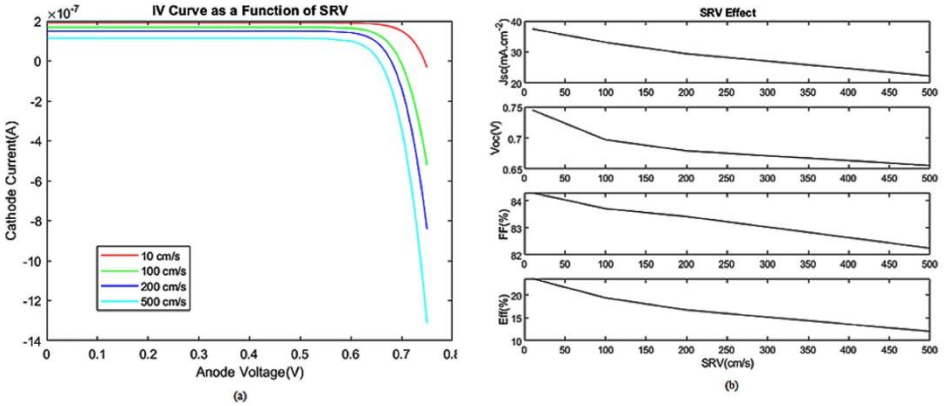

Fig. 4. Effect of SRV change on a) current-voltage curve b) Jsc, Voc, FF and η

According to Fig. 4(a), as the front SRV increases, the cell current and voltage decrease. Also, according to Fig. 4(b), the increase of front SRV leads to decreased Jsc. Because in this situation, more photocarriers recombine in trap levels. In the meantime, Voc also has a decreasing trend. Although, although the electric field increases due to the creation of space charge region on the surface of the cell, the electric potential decreases based on the relationship E(x)=(-dV(x)/dx). As Fig. 4(b), the increase in front SRV also led to a decrease in FF. As shown in Fig. 4(a), V_{mpp} and I_{mpp} decreased with the increase of SRV, resulting in the decrease of FF, according to (3). Finally, the efficiency also decrease due to the decrease of Jsc, Voc and FF. As a result, the optimal front SRV value for the proposed structure is 10 cm/s.

B. Effect of c-Si substrate thickness

More light absorption is the advantage of increasing the thickness of the c-Si substrate. Because the probability of absorbing shorter wavelengths that have more energy than the bandwidth of silicon increases. However, further recombination carriers are its downside. Because photocarriers, whose maximum photo generation rate is at the top of the cell near the front surface, have to move a longer distance to reach interdigitated back contacts, and this causes more recombination processes to occur for them in this distance. Therefore, due to this trade-off, an optimal thickness should be determined for it. Some research indicates that the optimal thickness is between 150-200 µm with a lifetime of 5-7 ms, an SRV of 10 cm/s and a resistivity of 1 Ω.cm [31] [32]. According to the mentioned information, in the proposed IBC-SHJ solar cell, the most optimal values for the thickness and lifetime of the carriers in the c-Si substrate are 150 µm and 7 ms, respectively. Also, the resistivity of this layer is considered equal to 1 Ω.cm.

C. Effect of c-Si substrate doping concentration

The current-voltage curve and graphs of Jsc, Voc, FF and η according to the change of doping concentration of c-Si substrate are presented in Fig. 5.

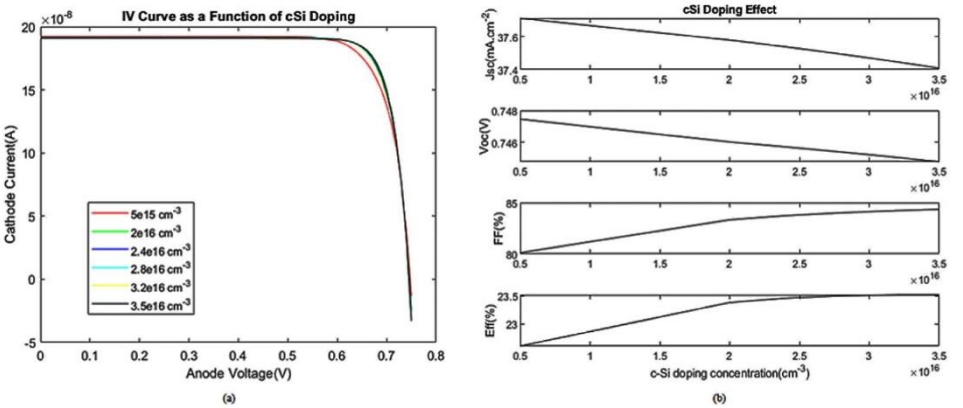

Fig. 5. Effect of c-Si substrate doping concentration on a) current-voltage curve b) Jsc, Voc, FF and η

According to Fig. 5(a), the increase in c-Si substrate impurity, decreases the cell current. On the other hand, increasing the doping concentrations of c-Si substrate has less effect on the cell voltage. In fact, in higher doping concentration, the lifetime of the carriers and their mobility decreases. In this situation Auger recombination occurs more than before, which reduces the cell current. The reduction of Jsc under the influence of the mentioned processes, in Fig. 5(b), is inevitable. Meanwhile, Voc also experiences a decreasing trend with a tiny slope, and it can be ignored for the same reason as for Voc in Fig. 5(a). According to the FF graph, increasing the doping concentration of c-Si substrate leads to an increase in FF. Because Isc decreases, FF increases according to relation (3).

According to the η graph, a significant increase in FF ultimately leads to an increase in efficiency. This is while, increasing the doping concentration of c-Si substrate up to 3.4×10^{16} cm^{-3}, the efficiency of the cell increases and then decreases. In fact, by increasing the doping concentration of the c-Si substrate to a power of more than 10^{16} cm^{-3}, the probability of scattering mechanisms increases, which leads to a decrease in cell efficiency. Therefore, in the proposed solar cell, the most optimal value for the c-Si substrate doping concentration is equal to 3.4×10^{16} cm^{-3}.

D. Effect of thickness and doping concentration of i-a-Si layer

1) Effect of i-a-Si layer thickness

To recent research, the existence of the hydrogenated i-a-Si buffer layer with the back surface passivation effect in the IBC-SHJ cell significantly improves the

open-circuit voltage and short-circuit current [33]. However, simultaneously, it leads to a decrease in fill factor [23]. Therefore, in this research, it has been tried to increase the efficiency of the cell by depositing aforementioned layer using ATHENA. The current-voltage curve and the Jsc, Voc, FF and η graphs considering the variation of the i-a-Si layer thickness are presented in Fig. 6.

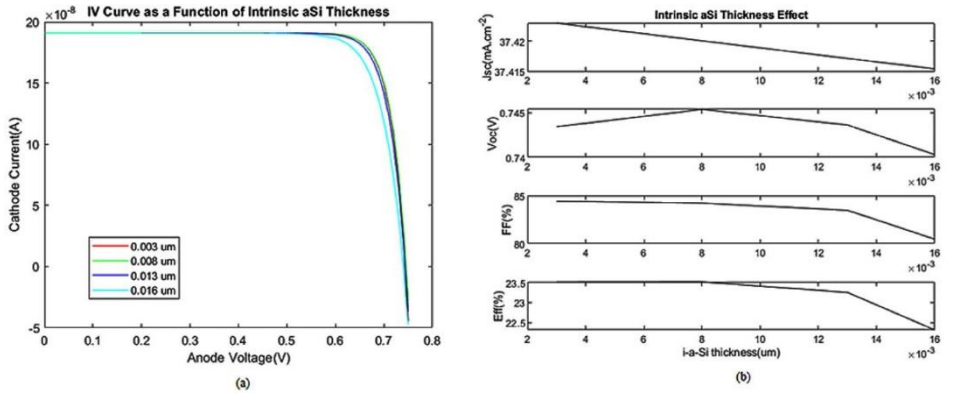

Fig. 6. Effect of i-a-Si layer thickness on a) current-voltage curve b) Jsc, Voc, FF and η

According to Fig. 6(a) and (b), it can be seen that increasing the thickness of the i-a-Si layer does not have a significant effect on Jsc and cell current. However, as the thickness of i-a-Si layer increases up to 0.008 µm, Voc increases slightly and then decreases with a slight slope. Because due to the increase of i-a-Si layer thickness up to 0.008 µm, the resistance increases and the potential on the buffer layer drops. Nevertheless, in thicknesses more than 0.008 µm, due to considering the maximum value of the built-in potential of the silicon junction equal to 0.75 V, the voltage will decrease. In the meantime, as i-a-Si layer thickness increases, the FF decreases. Because according to Fig. 6(a), increasing the i-a-Si layer thickness up to 0.008 µm increases Voc and after the thickness of 0.008 µm, V_{mpp} decreases. Therefore, according to relation (3), it can be said that FF decreases. A similar trend can be observed for cell Efficiency According to the simulation results, in the proposed IBC-SHJ solar cell, the most optimal value for i-a-Si layer thickness is 0.006 µm.

2) Effect of i-a-Si layer doping concentration

Current-voltage curve and Jsc, Voc, FF and η graphs considering the change of i-a-Si layer doping concentration are presented in Fig. 7.

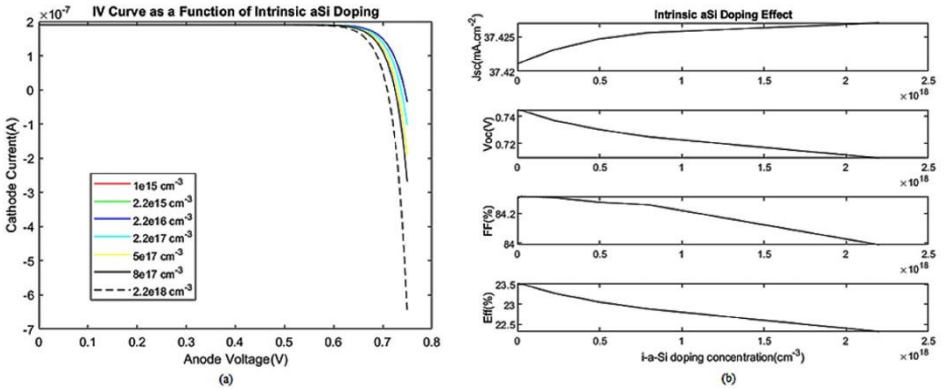

Fig. 7. Effect of i-a-Si layer doping concentration on a) current-voltage curve b) Jsc, Voc, FF and η

According to Fig. 7(a), increasing the doping concentration of i-a-Si layer has a decreasing effect on the cell voltage, however, doping concentration of the i-a-Si layer does not significantly affect the current. As shown in Fig. 7(b), increasing the doping concentration of i-a-Si layer, increases Jsc with a tiny slope. The increase in current with a step of 0.001 is slight and as seen in the current-voltage curves in Fig. 7(a), increasing the doping concentration of i-a-Si layer does not have much effect on cell current. According to the Voc graph in Fig. 7(b), the Voc decreases with increasing doping concentration of i-a-Si layer. Because the increased doping concentration, reduces the series resistance due to increase in free carriers. According to the FF graph, FF decreases with increasing the doping concentration of i-a-Si layer. Also, as shown in Fig. 7(a), V_{mpp} decreases with increasing the doping concentration of i-a-Si layer. Therefore, according to relation (3), FF also decreases. According to the η graph, the efficiency of the cell decreases with increasing the doping concentration of i-a-Si layer. It can be considered to reduce Voc and FF. As a result, in the proposed IBC-SHJ solar cell, the most optimal value for i-a-Si layer doping concentration is equal to 1×10^{15} cm^{-3}.

E. Effect of p-strip width

The current-voltage curve and Jsc, Voc, FF and η graphs considered with the change of p-strip width are presented in Fig. 8.

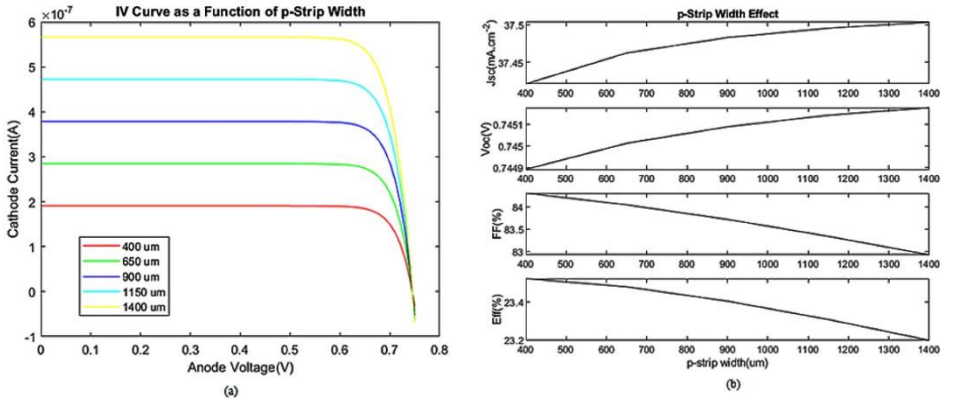

Fig. 8. Effect of p-strip width on a) current-voltage curve b) Jsc, Voc, FF and η

According to Fig. 8(a), it shown that increasing the width of p-strip, increases the current. Nevertheless, at the same time, it does not have much effect on the voltage. As shown in Fig. 8(b), Jsc increases with increasing the p-strip width. Because the width of metal contact is equal to the p-strip. On the other hand increasing the width of metal contact decreases the cell series resistance and thus, increases the cell current. Generally, in the IBC-SHJ structure, the p-strip width is set to be larger than the n-strip width. Holes are the minority carriers of the substrate. By choosing a larger width for the p-strip region, it will be possible to collect more minority carriers in the metal contacts. It significantly reduces the possibility of recombination in the substrate and this leads to an increase the cell current.

Meanwhile, Voc increases with increasing the p-strip width. However, the voltage increase is tiny and insignificant. As mentioned in Fig. 8(a), increasing the width of p-strip does not have much effect on the voltage. On the other hand, the FF decreases as the p-strip width increases. Because according to Fig. 8(a), increasing the width of p-strip, increases Isc. Therefore, according to relation (3), FF decreases. Also, the efficiency of the cell decreases with the increase of the p-strip width. Considering the simulation, the most optimal value for p-strip width is equal to 400 µm.

F. Effect of emitter doping concentration

The current-voltage curve and Jsc, Voc, FF and η graphs considering the change of doping concentration of the emitter region are presented in Fig. 9.

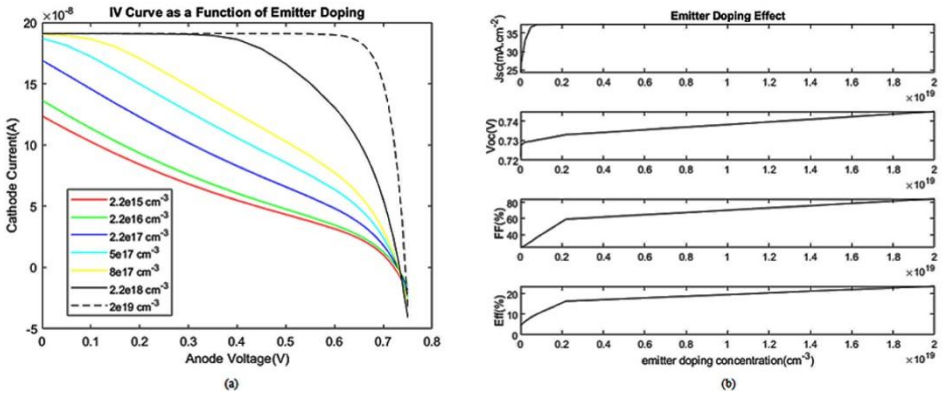

Fig. 9. Effect of emitter doping concentration on a) current-voltage curve b) Jsc, Voc, FF and η

According to Fig. 9(a), increasing the doping concentration of emitter region leads to increase in cell current, nevertheless, has little effect on the voltage. As shown in Fig. 9(b), increasing the doping concentration of emitter region, increases Jsc. In this situation, the number of free carriers and photocurrent increases. As concluded from the current-voltage curves in Fig. 9(a), increasing the doping concentration of emitter region increases Voc with a tiny slope. According to the FF graph, FF increases. Because with the increase of emitter region doping concentration, V_{mpp} and I_{mpp} increase and the curve is wholly S-shaped at the concentration of 2×1019 cm-3. Therefore, according to relation (3), FF increases. On the other hand, the cell efficiency increases due to an increase in Jsc, Voc and FF. As a result, the most optimal value for the doping concentration of emitter region is equal to 2×10^{19} cm^{-3}.

G. Effect of gap width between electrodes

The width of the gap between the electrodes is one of the critical parameters in controlling the current of the cell. Because it can lead to shunting the electrodes if it not adjusted accurately. On the other hand, its excessive increase reduces the photocurrent by reducing the optimal value of the n- and p-strip width and increasing the cell series resistance. Next, the current-voltage curve and Jsc, Voc, FF and η graphs considering the change of gap width between the electrodes are presented in Fig. 10.

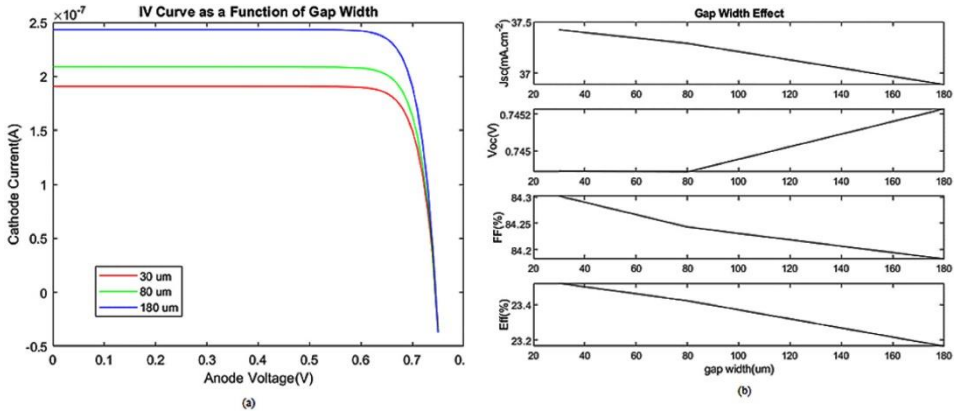

Fig. 10. Effect of gap width between the electrodes on a) current-voltage curve b) Jsc, Voc, FF and η

According to Fig. 10(a), increasing the gap width between the electrodes leads to an increase the current however, does not have a significant effect on the voltage. As shown in Fig. 10(b), Jsc decreases with increasing gap width. In fact, the gap region between the electrodes has an essential effect on the photocurrent in the cell by influencing the n- and p-strip width. On the other hand, due to the increase cell resistance, Voc increases with a low slope.

According to Fig. 10(a), as the gap width increases, Isc increases and thus, FF decreases. Also, cell efficiency decreases. Because the recombination of the minority carriers between the p- and the n-strip increases due to the increase in the lateral distance traveled. In other words, the increase of the gap width corresponds to an additional lateral distance for the minority photocarriers generated in the c-Si substrate and in the upper part of the n-strip (according to Fig. 2(a)). This extra distance increases the probability of recombination before reaching the p-strip. In addition, by increasing the width of the gap between the electrodes, the possibility of recombination at the interface between the c-Si substrate and the gap region increases. Therefore, according to all reasons mentioned above, the gap width should be set as low as possible to obtain the optimal value for cell efficiency. As a result, the most optimal value for the gap width equal to 30 µm is obtained.

H. Effect of n-strip width

The current-voltage curve and Jsc, Voc, FF and η graphs with changing the n-strip width are presented in Fig. 11.

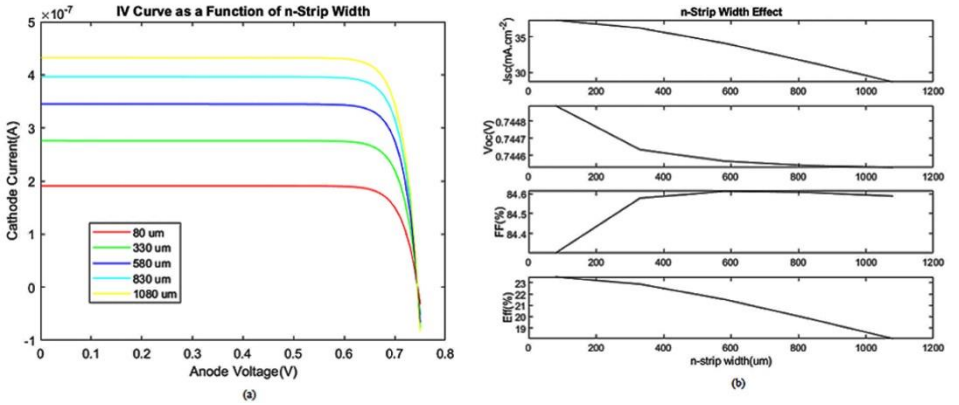

Fig. 11. Effect of n-strip width on a) current-voltage curve b) Jsc, Voc, FF and η

According to Fig. 11(a), it can be concluded that increasing the n-strip width increases the cell current. Nevertheless, it has little effect on the voltage. In this situation, due to the increase in the average lateral distance that the minority carriers must travel to reach the p-strip, Jsc decreases and increases the probability of carrier recombination and decreases the cell current. According to the Voc graph, Voc decreases with a slight slope. As the n-strip width increases to 580 µm, FF increases and then decreases. Because its increase up to 580 µm, increases the I_{mpp} and for more than 580 µm, Isc increases. Therefore, according to (3), it can be seen that FF increases until reaching a width of 580 µm and then decreases from this value. On the other hand, the efficiency decreases with the decrease of Jsc. Therefore, the n-strip should be set as low as possible to obtain the best Jsc values. In fact, a larger width leads to an increase in series resistance against the current of majority carriers (electrons). As a result, the most optimal value for the n-strip width is equal to 80 µm.

I. Effect of BSF doping concentration

The current-voltage curve and Jsc, Voc, FF and η graphs considered with the change of BSF region doping concentration are presented in Fig. 12.

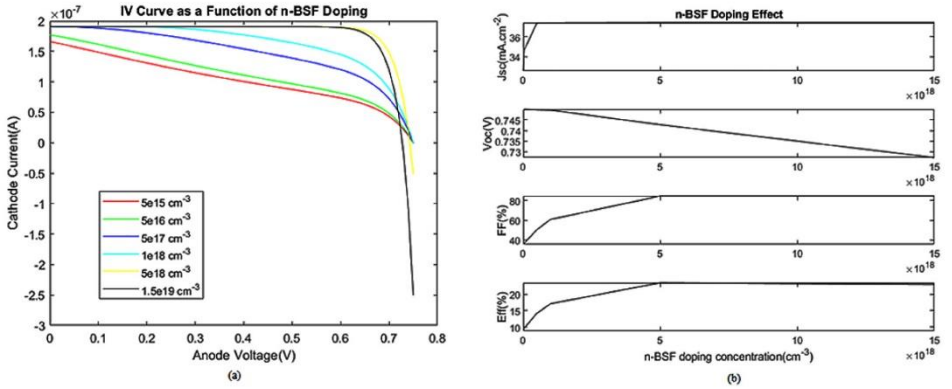

Fig. 12. Effect of BSF doping concentration on a) current-voltage curve b) Jsc, Voc, FF and η

According to Fig. 12(a), it can be seen that increasing the doping concentration of BSF region increases the cell current. Also, as the concentration of this region increases, the voltage decreases. In this situation due to increase of free carriers and photocurrent of the cell Jsc increases and Voc decreases and the series resistance decreases. On the other hand, with the increase of doping concentration in the BSF region, the FF increases. Because according to Fig. 12(a), V_{mpp} and I_{mpp} increase and according to the relation (3) FF increases. Also, the cell efficiency increases up to 4.3×10^{18} cm^{-3} and decreases afterward. In fact, to reduce the series resistance behind the cell, the doping concentration of the BSF region should be increased as much as possible. However, on the other hand, the excessive increase of doping concentration in the BSF region leads to the increase of scattering mechanisms for the carriers, which reduces the cell efficiency. Therefore, in the proposed IBC-SHJ solar cell, the most optimal value for the doping concentration of BSF region is equal to 4.3×10^{18} cm^{-3}.

In Table II, the output electrical characteristics of proposed IBC-SHJ solar cell compared to some previous similar structures.

TABLE II
THE OUTPUT ELECTRICAL CHARACTERISTICS OF THE PROPOSED IBC-SHJ SOLAR CELL COMPARED TO PREVIOUS SIMILAR STRUCTURES

Ref.	V_{OC} (mV)	FF (%)	J_{SC} (mA.cm^{-2})	η (%)
[14]	635	77.7	39.2	19.4
[16]	726.7	-	39.95	23.31
[17]	671	77.70	40.05	20.88
[19]	701	78.05	37.32	20.43
[20]	723	83.51	38.37	23.20
[Proposed structure]	745	84.30	37.42	23.52

5. CONCLUSION

In this research, the effect of the deposition parameters of the IBC-SHJ cell, including the front SRV, the thickness and doping concentration of the c-Si substrate, the thickness and doping concentration of i-a-Si layer, the doping concentration of emitter region, the width and doping concentration of the n- and p-strip, the gap width between electrodes and the doping concentration of BSF region on the output characteristics of the solar cell were investigated. Our optimized IBC-SHJ solar cell yields a short-circuit current density of 37.42 mA/cm^2 and open-circuit voltage of 745 mV with cell efficiency of 23.52% having a fill factor of 84.30 under AM1.5G without any extra ARCs and more structural periodicity. Thus, a simple structure with improved conversion efficiency is proposed. The simulated results yielded an improvement of about 22 mV for the open-circuit voltage, 0.8 for the fill factor, and about 1.38% for the cell efficiency compared to the conventional cell without optimizing cell parameters. Simulation shows that cell efficiency varies due to the change in thickness and doping concentration of some layers and so these parameters are improved accordingly. According to the results, the optimum thickness of c-Si substrate and the i-a-Si layer is equal to 150μm and 0.006μm respectively. Also the optimum width of p-strip, gap between electrodes and n-strip is equal to 400 μm, 30 μm and 80 μm respectively. On the other hand, the optimum doping concentration of the c-Si substrate and i-a-Si layer is equal to 3.4×10^{16} cm^{-3} and 1×10^{15} cm^{-3} respectively. Also, the optimum doping concentration of emitter and BSF regions is equal to 2×10^{19} cm^{-3} and 4.3×10^{18} cm^{-3} respectively. In addition, the analysis of the electric field distribution in the cell and the investigation of the transport of photocarriers towards the back contacts were presented in details. In fact, the design of two space charge areas in the upper and lower parts of the cell,

in addition to prevent the recombination of photocarriers, leads to drift them towards the interdigitated back contacts. The existence of an anti-reflective coating with the opposite concentration of the substrate, by creating a space charge region in the front part of the cell, prevents the recombination of photocarriers and drifts them towards the back contacts of the cell. In addition to the upper area of the cell, near the back contacts, due to the back p-n junction, another region of space charge is created, which facilitates the drift of carriers towards the anode and cathode electrodes and prevents their recombination. The photocarriers generated in the front part of the cell are drifted towards the contact of the same name under the influence of the electric field of the space charge region. Photocarriers travel vertically towards the back contacts, in the cell body and horizontally near the contacts. Meanwhile, increasing the cell width increases the recombination probability and decreases the photocurrent and cell efficiency. According to the results of the physical analysis of the device, the electric field near the back contacts to increase the carrier collection rate in the metal contacts and decreases the recombination rate.

REFERENCES

[1] C. N Kruse, S. Schafer, F. Haase, V. Mertens, H. Schulte-Huxel, B. Lim, B. Min, T. Dullweber, R. Peibst, R. Brendel. *Simulation-based roadmap for the intergration of poly-silicon on oxide contacts into screen-printed crystalline silicon solar cells*. Nature research. 11(2021) 996. Available: https://doi.org/10.1038/s41598-020-79591-6.

[2] T. Allen, J. Bullock, X. Yang, A. Javey, S. De Wolf. *Passivating contacts for crystalline silicon solar cells*. Nature Energy. 4(11) (2019) 914-928. Available: https://doi.org/10.1038/s41560-019-0463-6.

[3] M. Shakiba, A. Kosarian, E. Farshidi. *Effects of processing parameters on crystalline structure and optoelectronic behavior of DC sputtered ITO thin film*. J Mater Sci: Mater Electron. 28(2016) 787–797. Available: https://doi.org/10.1007/s10854-016-5591-1.

[4] M. Rajaee, S. Rabiee. *Analysis and implementation of a new method to increase the efficiency of photovoltaic cells by applying a dual axis sun tracking system and Fresnel lens array*. Optoelectronical Nanostructures. 6(3) (2021) 59-80. Available: https://doi.org/10.30495/JOPN.2021.28531.1229.

[5] A. Mahmoudloo. *Investigation and simulation of recombination models in virtual organic solar cells*. Optoelectronical Nanostructures. 7(4) (2022) 1-12. Available: https://doi.org/10.30495/jopn.2022.30243.1263.

[6] M. Roohollahi, M. R Shayesteh, M. Pourahmadi. *Improved perovskite solar cell performance using semitransparent CNT layer*. Optoelectronical Nanostructures. 8(1) (2023) 32-46. Available: https://doi.org/10.30495/JOPN.2023.29770.1253.

[7] A. Kosarian, M. Shakiba, E. Farshidi. *Role of hydrogen treatment on microstructural and opto-electrical properties of amorphous ITO thin films deposited by reactive gas-timing DC magnetron sputtering*. J Mater Sci: Mater Electron. 28(2017) 10525–10534. Available: https://doi.org/10.1007/s10854-017-6826-5.

[8] M. Shakiba, M. Shakiba. *Role of Critical Processing Parameters on Fundamental Phenomena and Characterizations of DC Argon Glow Discharge*. Optoelectronical Nanostructures. 7(2022) 67-91. Available: https://doi.org/10.30495/JOPN.2022.29878.1255.

[9] A. Kosarian, M. Shakiba, E. Farshidi. *Role of sputtering power on the microstructural and electro-optical properties of ITO thin films deposited using DC sputtering technique*. IEEJ Transaction on Electrical and Electronic Engineering. 13(2018) 27–31. Available: https://doi.org/10.1002/tee.22494.

[10] C. Hollemann, F. Hasse, M. Rienacker, V. Barnscheidt, J. Krugener, N. Folchert, R. Brendel, S. Ritcher, S. Grober, E. Sauter, J. Hubner, M. Oestreich, R. Peibst. *Separating the two polarities of the POLO contacts of an 26.1%-efficient IBC solar cell*. Natureresearch. 10(2020) 658. Available: https://doi.org/10.1038/s41598-019-57310-0.

[11] F. Ghavami, A. Salehi. *High-efficiency CIGS solar cell by optimization of doping concentration, thickness and energy band gap*. Modern Physics Letters B. 34(4) (2020) 2050053. Available: https://doi.org/10.1142/S0217984920500530.

[12] Q. Pengcheng, Q. Pengxiang. *Characteristics and development of interdigitated back contact solar cells*. IOP Conf. Series: Earth and Environmental Science. 621(2021) 012067. Available: https://doi.org/10.1088/1755-1315/621/1/012067.

[13] R. Hosseini, M. Bahramgour, N. Delibas, A. Niaei. *A simulation study around investigating the effect of polymers on the structure and performance*

of a perovskite solar cell. Optoelectronical Nanostructures. 7(2) (2022) 37-50. Available: https://doi.org/10.30495/JOPN.2022.29720.1252.

[14] J. Haschke, Y. Y Chen, R. Gogolin, M. Mews, N. Mingirulli, L. Korte, B. Rech. *Approach for a simplified fabrication process for IBC-SHJ solar cells with high fill factors.* Energy Procedia. 38 (2013) 732-736. Available: https://doi.org/10.1016/j.egypro.2013.07.340.

[15] V. Giglia, R. Varache, J. Veirman, E. Fourmond. *Influence of cell edges on the performance of silicon heterojunction solar cells*. Solar Energy Materials and Solar Cells. 238(2022) 111605. Available: https://doi.org/10.1016/j.solmat.2022.111605.

[16] A. R. M Rais, S. Sepeai, M. K. M Desa, M. A Ibrahim, P.J Ker, S. H Zaidi, K. Sopian. *Photo-generation profiles in deeply-etched, two-dimensional patterns in interdigitated back contact solar cells.* Journal of Ovonic Research. 17(3) (2021) 283-289. Available: https://doi.org/10.15251/jor.2021.173.283.

[17] X. Li, A. Liu. *Carrier transmission mechanism-based analysis of front surface field effects on simplified industrially feasible interdigitated back contact solar cells*. Energies. 13(2020) 5303. Available: https://doi.org/10.3390/en13205303.

[18] M. D Lammert, R. J Schwartz. *The interdigitated back contact solar cell: a silicon solar cell for use in concentrated sunlight*. IEEE Trans. Electron Devices. 24(1977) 337–342. Available: https://doi.org/10.1109/t-ed.1977.18738.

[19] Silvaco. *2D IBC-SHJ solar cell simulation and optimization.* (2013). Available: https://silvaco.com.

[20] M. Belarbi, M. Beghdad, A. Mekemeche. *Simulation and optimization of n-type interdigitated back contact silicon heterojunction (IBC-SiHJ) solar cell structure using Silvaco Tcad Atlas*. Solar Energy. 127(2016) 206-215. Available: http://doi.org/10.1016/j.solener.2016.01.020.

[21] K. Yoshikawa, H. Kawasaki, W. Yoshida, T. Irie, K. Konishi, K. Nakano, T. Uto, D. Adachi, M. Kanematsu, H. Uzu, K. Yamamoto. *Silicon heterojunction solar cell with interdigitated back contacts for a photoconversion efiiciency*. Nature Energy. 2(20) (2017) 17032. Available: http://doi.org/10.1038/nenergy.2017.32.

[22] J. Bao, A. Liu, Y. Lin, Y. Zhou. *An insight into effect of front surface field on the performance of interdigitated back contact silicon heterojunction solar*

cells. Materials Chemistry and Physics. 255(2020) 123625. Available: https://doi.org/10.1016/j.matchemphys.2020.123625.

[23] M. Lu, U. Das, S. Bowden, S. Hegedus, R. Birkmire. *Optimization of interdigitated back contact silicon heterojunction solar cells by two-dimensional numerical simulation*. Institute of Energy Conversion, Univesity of Delaware, Newark, DE 19716 U.S.A, IEEE. (2009). Available: https://doi.org/10.1109/pvsc.2009.5411332.

[24] T. Sawada, N. Terada, S. Tsuge, T. Baba, T. Takahama, K. Wakisaka, S. Tsuda, S. Nakano. *High-efficiency a-Si/c-Si heterojunction solar cell*. In: Proceedings of 1994 IEEE 1st World Conference on Photovoltaic Energy Conversion, Waikoloa, USA. (1994) 1219–1226. Available: https://doi.org/10.1109/wcpec.1994.519952.

[25] N. Jensen, R. M Hausner, R. B Bergmann, J. H Werner, U. Rau. *Optimization and characterization of amorphous/crystalline silicon heterojunction solar cells*. Prog. Photovolt. Res. Appl. 10(2002) 1–13. Available: https://doi.org/10.1002/pip.398.

[26] M. A Green. *Solar Cells: Operating principle*. (1982) 2. Available: https://doi.org/10.1016/0038-092x(82)90265-1.

[27] F. Granek, M. Hermle, C. Reichel, A. Grohe, O. Schultz-Wittmann, S. Glunz. *Positive effects of front surface field in high-efficiency back-contact back-junction n-type silicon solar cells.* PVSC '08. 33rd IEEE, pp.1-5. Available: https://doi.org/10.1109/pvsc.2008.4922759.

[28] Z. Q Zhou, F. Hu, W. J Zhou, H. Y Chen, L. Ma, C. Zhang, M. Lu. *An investigating on a crystalline-silicon solar cell with black silicon layer at the rear.* Nanoscale Research Letters. 12(2017) 623. Available: https://doi.org/10.1186/s11671-017-2388-y.

[29] D. Diouf, J. P Kleider, C. Longeaud. *Two-dimensional simulations of interdigitated ack contact silicon heterojunctions solar cells.* Chapter 15 of the book physics and technology of amorphous-crystalline silicon heterostructure solar cells. Springer. (2011) 483-519. Available: https://doi.org/10.1007/978-3-642-22275-7_15.

[30] P. Taylor, A.I Lvovsky. *Fresnel Equations*. Encycl. Opt. Eng., no. August, (2013) 37–41. Available: https://doi.org/10.1081/E-EOE-120047133.

[31] F. Granek. *High-efficiency back-contact back-junction silicon solar cells*. Fraunhofer institut für solare energiesysteme, Freiburg im Breisgau: Albert-

Ludwigs-Universität. (2009) 209. Available: https://www.researchgate.net/publication/43033375.

[32] A. J McEvoy, L. Castañer, T. Markvart. *Solar cells: materials, manufacture and operation*. Second Edition ed.: Elsevier. (2012). Available: https://elsevier.com.

[33] D. D Smith, H. C Luan, J. Manning, T. D Dennis, A. Waldhauser, K.E Wilson, G. Harley, W. P Mulligan. *Generation 3, Improved performance at lower cost*. In: proceedings of 35th IEEE PV SC. (2010) 275–278. Available: https://doi.org/10.1109/pvsc.2010.5615850.